Check for updates

Band gap tuning and enhanced photosensitivity of nitrogenated TiO$_2$ *via* graphene incorporation for low-voltage UV photodetectors

David O. Idisi, [ID] *[a] Mosimo Kgomo,[b] Daniel C. Chilukusha,[ac] Bonex W. Mwakikunga[ab] and Joseph K. O. Asante [ID] [a]

The emergence of metal oxide-based photodetectors has been on the rise in recent years, owing to the tunability of their optical band gap and photosensitivity. The current study focuses on tuning the band gap of nitrogenated TiO$_2$ (N–TiO$_2$) using reduced graphene oxide. The incorporation of low doses of graphene (0.0394 and 0.0432 g) into the N–TiO$_2$ shows widening of the band gap (2.52 → 2.79 → 2.95 eV). The electrical conductivity properties obtained from the current–voltage sweep show a decrease as the graphene concentration increases and are consistent with the widening of the band gap. The photosensitivity properties of a high concentration of graphene-supported N–TiO$_2$ depict improved response at low voltage (0.5 V) in comparison to pristine N–TiO$_2$ by 14.7%, which suggests that graphene incorporation supports photodetection at low voltage. The study proposes that incorporating graphene into N–TiO$_2$ nanostructures can be used to enhance the sensitivity of low-voltage UV photodetector devices.

Introduction

The importance of photodetectors in powering various devices and applications has become increasingly significant in today's technology-based economies. Photodetectors such as UV-range type are useful for applications in environmental monitoring, infrared telecommunication and crucial for health and agriculture sectors.[1–3] The recent and ongoing growth of technology can be attributed to the optical sensitivity properties as well as the low-voltage performance of the materials being used for the device fabrication. The currently available technology is mainly the silicon- and germanium-based photodetectors, which rely on chemical bonding structures and intrinsic visible-blindness.[4] While strong reliability and performance have positioned Si-based UV photodetectors above diamond, SiC, III-nitrides, and III–V compounds, silicon has a direct band gap (1.75 eV) that is not tunable, resulting in low absorption.

Metal oxides are a class of materials that have proven efficiency for optical-based devices, owing to their band gap tunability. The ease of the optical band gap tuning of metal oxides has led to their use in applications such as organic solar cell harvesting,[5] photoresist patterning[6] and photodetectors.[7] Among the numerous metal oxides (ZnO, NiO, Ga$_2$O$_3$, Fe$_3$O$_4$),

TiO$_2$ has been a frontrunner, owing to ease of synthesis and electronic properties. Additionally, the electronic structure comprises a mixed crystal structure, such as a TiO$_6$ octahedron. The octahedra block structures enable strong coupling and hybridization, leading to mixed phases such as rutile, anatase, titania and mixed rutile-anatase phases.[8]

While the wide band gap of anatase TiO$_2$ (∼3.2 eV) could be trivial for UV absorption,[9] the incorporation of defects by tuning its band gap could enable improved photosensitivity. The use of doping/functionalization of TiO$_2$ with other nanomaterials is not a novel subject and has proven effective in improving its properties in various applications.[9–11] Moreover, the systemic use of nitrogen in the doping/functionalization of TiO$_2$ has proven effective in tuning its bandgap. For instance, a recent study by Lim *et al.*[12] demonstrated the possibility of narrowing the bandgap of TiO$_2$ (3.02 → 2.07 eV) for photocatalysis applications. Furthermore, carbon-based functionalization is another route to tune the bandgap of metal oxides. Graphene, which is a 2D hexagonal sp^2/sp^3-C hybridized carbon nanomaterials has shown immense potential for improving electrical conductivity of parent metal oxides. The high electron mobility of graphene has been widely useful in inducing defects within the bandgap region of metal oxides, thereby improving the selectivity and performance of optoelectronic device applications.[13]

Graphene-supported nitrogen-doped TiO$_2$ has been widely investigated for sensor and photocatalytic applications.[14,15] However, this material system remains underexplored for photodetector applications. Unlike photocatalysis, which

aDepartment of Physics, Tshwane University of Technology, Pretoria, South Africa. E-mail: efedave26@gmail.com

bDST-CSIR Centre for Nanostructured and Advanced Materials, Council of Scientific and Industrial Research, Pretoria, 0001, South Africa

cDepartment of Physics, Mulungushi University, Kabwe, 10101, Zambia

typically requires bandgap narrowing of TiO$_2$ to enhance visible-light absorption for efficient electron–hole generation, UV photodetectors benefit from a wider bandgap to ensure visible blindness and improved UV selectivity. The few existing reports on graphene–TiO$_2$ photodetectors[14] predominantly employ layered heterojunction configurations (TiO$_2$ on graphene or *vice versa*) rather than composite structures. In this work, nitrogen doping and graphene incorporation were synergistically employed to tune the electronic structure of TiO$_2$ for enhanced photoconductivity. The composite design promotes efficient interfacial charge transfer and improved carrier mobility, thereby enabling low-voltage, high-sensitivity UV detection.

Materials and experimental details

Anatase titanium(IV) oxide (99.8%), carbonyldiamine (urea) solution and reduced graphene oxide (rGO) powder were procured from Sigma-Aldrich. The synthesis process using the procured chemicals was carried out without further processing. Nitrogenated TiO$_2$ (N–TiO$_2$) and graphene-supported nitrogenated TiO$_2$ (N–TiO$_2$/G) were synthesized using both sol–gel and hydrothermal approaches.

Firstly, 5 g of titanium(IV) oxide powder was dispersed in 20 ml of urea solution in a 250 ml beaker. The solution was sonicated for 30 min to obtain a homogeneously dispersion solution. The solution was separated into three parts in three separate beakers. 0.0394 g and 0.0432 g of rGO were mixed with two parts of the N–TiO$_2$ solution and sonicated for 20 minutes to obtain N–TiO$_2$/G composite. The three sample solutions were transferred to a 150 mL Teflon-lined stainless-steel autoclave and heated at 120 °C for 12 h. The cooled, hydrothermally obtained solution was washed six times with ethanol and deionized water. The obtained precipitate was dried at 60 °C. The obtained powder samples were labelled as N–TiO$_2$, N–TiO$_2$/G1, and N–TiO$_2$/G2 and stored in an oven overnight.

Fabrication and characterization of nitrogenated and graphene-supported N–TiO$_2$ photodetector

Powders of N–TiO$_2$ and N–TiO$_2$/C samples were dissolved in deoxidized water and physically deposited on SiO$_2$/Si-based thin film as depicted in Fig. 1. The thin films were oven-dried at 40 °C with Ag-tape contacts applied afterwards to establish junction characteristics features. The illumination source consists of a Xenon lamp set at 50 W, whereas the electrical conductivity component was set up using the Keithley 2460 source-meter unit (SMU) controlled with the remote mode of 1.5.5 version of the 'SweepMe!' software.[15]

The microstructure and preliminary electronic properties of N–TiO$_2$ and graphene-supported N–TiO$_2$ were characterized using the Malvern Panalytical diffractometer (wavelength λ = 1.54 nm) and Horiba Raman spectrometer, respectively.
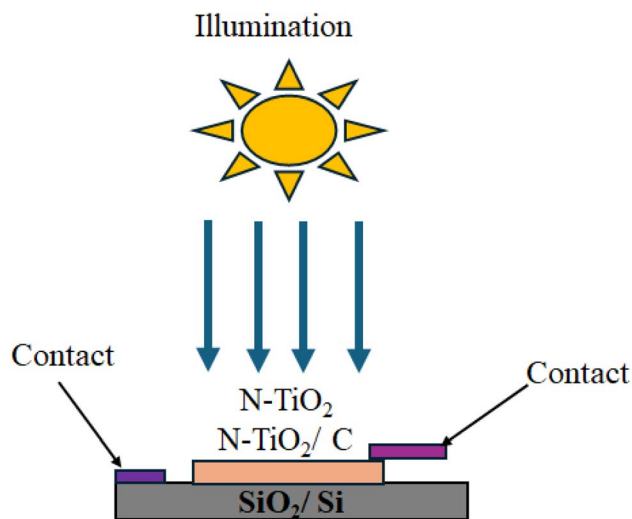

Fig. 1 The schematics of the fabricated device and characterization process of N–TiO$_2$ and graphene-supported N–TiO$_2$.

Results and discussions

The microstructure properties of N–TiO$_2$ and graphene-supported N–TiO$_2$, as measured in XRD, are shown in Fig. 2. The microstructure depicts peaks that are associated with JCPDS card no: 21-1272 (ref 16), where the indexed peaks are (101), (004), (200), (105), (211) and (204). The other peaks indexed as (111), *(200), (220) and (311) are associated with crystalline titanium nitride (TiN). The TiN peak positions are consistent with JCPDS card 38-1420 (ref 17) and indicates that part of the anatase phase has been transformed to Titania through the nitrogenation process.

The peak indexed as #(110) is associated with residual urea in the nitrogenated-TiO$_2$. The other residual peaks indicated by ** can be attributed to partial formation of the rutile phase, owing to the reaction from the carbonyldiamine (carbon)
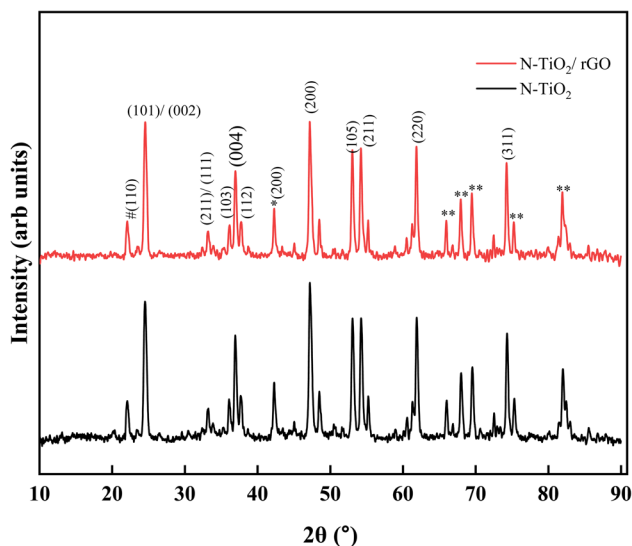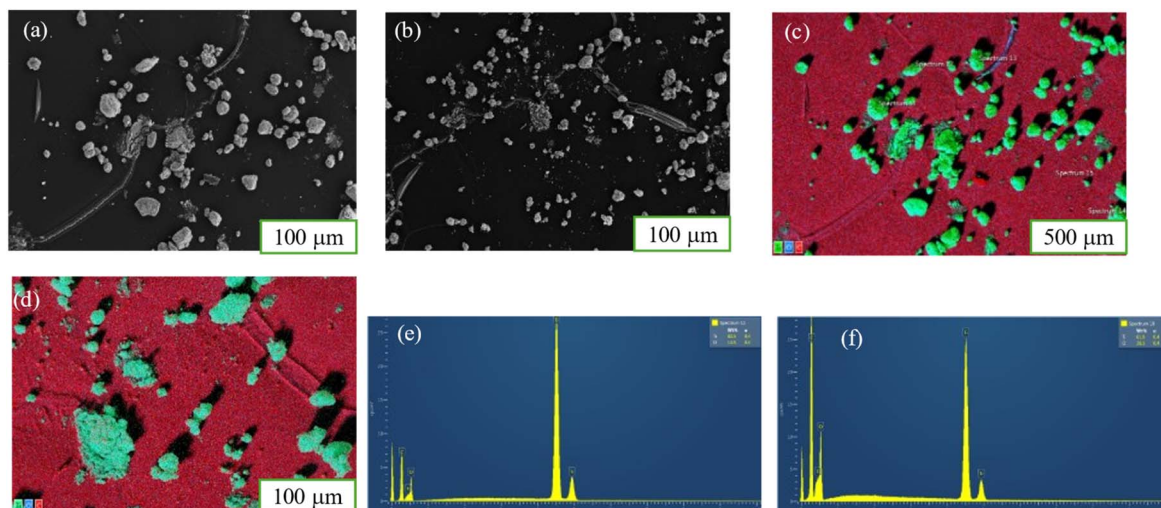

Fig. 2 The XRD spectra of nitrogenated TiO$_2$ and graphene-supported N–TiO$_2$.

Fig. 3 The SEM mapped images and EDX spectra of nitrogenated TiO_2 and graphene-supported $N-TiO_2$. (a) $N-TiO_2$ (b) graphene supported $N-TiO_2$ (c) and (d) mapped images of pristine and graphene supported $N-TiO_2$ (e) and (f) EDX spectra of $N-TiO_2$ and graphene supported $N-TiO_2$.

Table 1 The atomic percentage quantification of $N-TiO_2$ and graphene-supported $N-TiO_2$

| Samples	Atomic percentages			
	Ti 2p	C 1s	O 1s	N 1s
$N-TiO_2$	25.49	13.37	54.61	6.53
$N-TiO_2$/G1	23.08	14.83	60.21	1.9
$N-TiO_2$/G2	22.93	16.7	58.04	2.25

source.[18] Hence, it can be proposed that the nitrogenated TiO_2 has a highly crystalline structure with mixed phases of anatase and Titania. The incorporation of graphene as support material shows a C(002) peak overlap with Ti(101),[19] suggesting the diffusion of carbon atoms into the Titania compound. While the incorporation of urea improves the crystallinity of TiO_2, the formation of the different phases suggests non-stoichiometric features that inhibit the singular titanate phase.

The morphology of $N-TiO_2$ and $N-TiO_2$/G supported graphene as depicted by scanning electron microscopy (SEM), is shown in Fig. 3a and b, respectively. The distribution of Ti particles is dispersed across the surface of the material with minimal agglomeration. The incorporation of graphene shows increased dispersion of the particles. Based on the mapping of the SEM images shown in Fig. 3(c) and (d), the Ti particles are prominent on top of the carbon sheet. The appearance of carbon in pristine $N-TiO_2$ can be attributed to the carbon content in the urea solution, as well as the carbon coating used in charging reduction during the measurement.

Energy-dispersive X-ray spectroscopy (EDX) mapping of the SEM images of $N-TiO_2$ (Fig. 3(e)) and graphene-supported $N-TiO_2$/G (Fig. 3(f)) shows minimal carbon presence due to carbon coating and urea, whereas the increased carbon peak suggests the presence of graphene in the $N-TiO_2$ material. The elemental composition is further iterated in XPS quantification, shown in Table 1.

The particle size distribution of the SEM images for $N-TiO_2$ (a) and graphene-supported $N-TiO_2$ (b) is shown in Fig. 4, where the mean particle size is within a 20 μm range. Since there is no significant change in the average particle size of $N-TiO_2$ after rGO incorporation, it implies the carbon support provides diffusion support for the $N-TiO_2$ rather than lattice distortion.
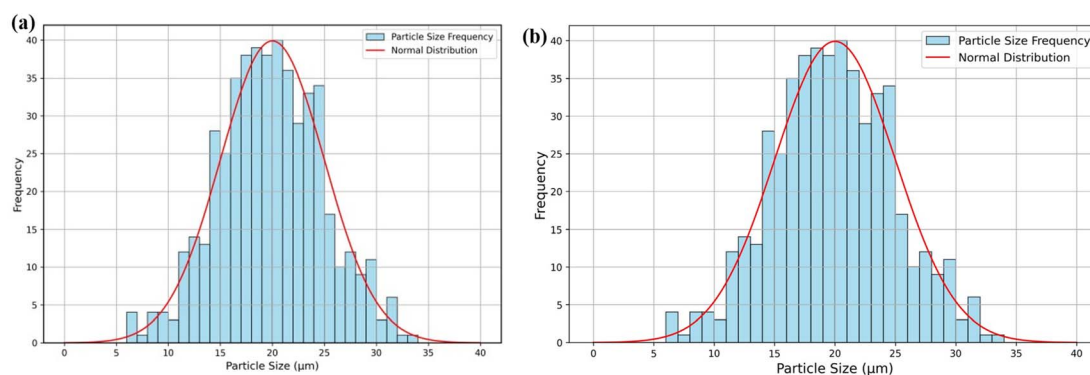
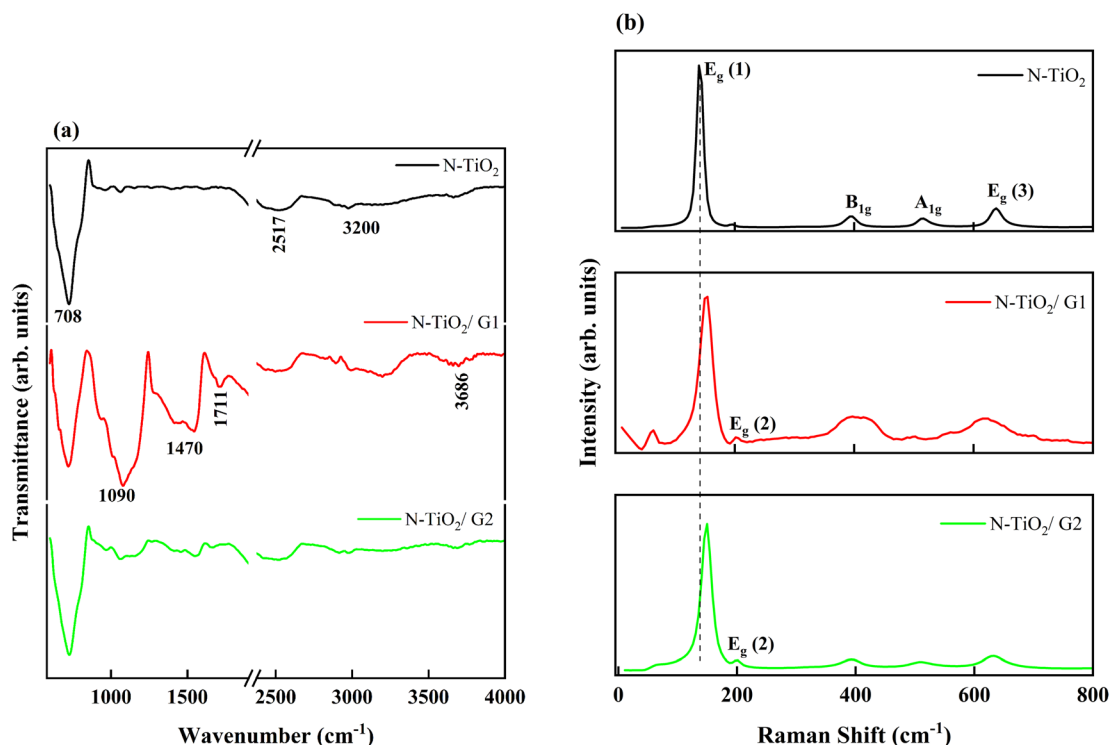**Fig. 4** Particle size distribution of (a) nitrogenated TiO_2 and (b) graphene supported $N-TiO_2$.

Fig. 5 (a) FTIR spectra of N−TiO₂ and graphene supported N−TiO₂/G and Raman spectra of N-TiO₂ and graphene supported N-TiO₂.

The behaviour is evident in the peak retention in the XRD spectra shown in Fig. 2.

The electronic bonding structure supporting the EDX was further analyzed using FTIR. Fig. 5(a) shows the FTIR of N–TiO₂ and graphene-supported N–TiO₂ for the two concentrations of graphene. Pristine N–TiO₂ shows transmittance at 708, 2517 and 3200 cm⁻¹. The peak position at 708 cm⁻¹ is attributed to the Ti–O–Ti bonding framework.[20] The 2517 and 3200 cm⁻¹ are attributable to C–H and –OH bond stretch, respectively.[21]

The incorporation of graphene is evidenced by the emergence of bands at 1090, 1470 and 1711 cm⁻¹, which are attributed to phenolic C–O–H stretching, alcoholic C–OH bending and C=C/C=O bond stretching, respectively.[22] The graphene

concentration increase (N–TiO₂/G2) shows a decrease in the oxygroup related component and enhancement of the Ti–O–Ti bonding framework, suggesting increased Ti-based reaction activities. These oxygen-containing functional groups render the possibility of covalent linkage of TiO₂ onto the rGO surface. During hydrothermal treatment, GO undergoes partial reduction. The observed decrease in the intensity of oxygen-related bands in the sample with higher graphene content (N–TiO₂/G2) may therefore be attributed to a greater degree of hydrothermal reduction, which removed these oxygen functionalities.

The Raman vibration modes have proven effective in probing the electronic properties of materials and identifying characteristic features of N–TiO₂. Fig. 4(b) shows the Raman spectra of
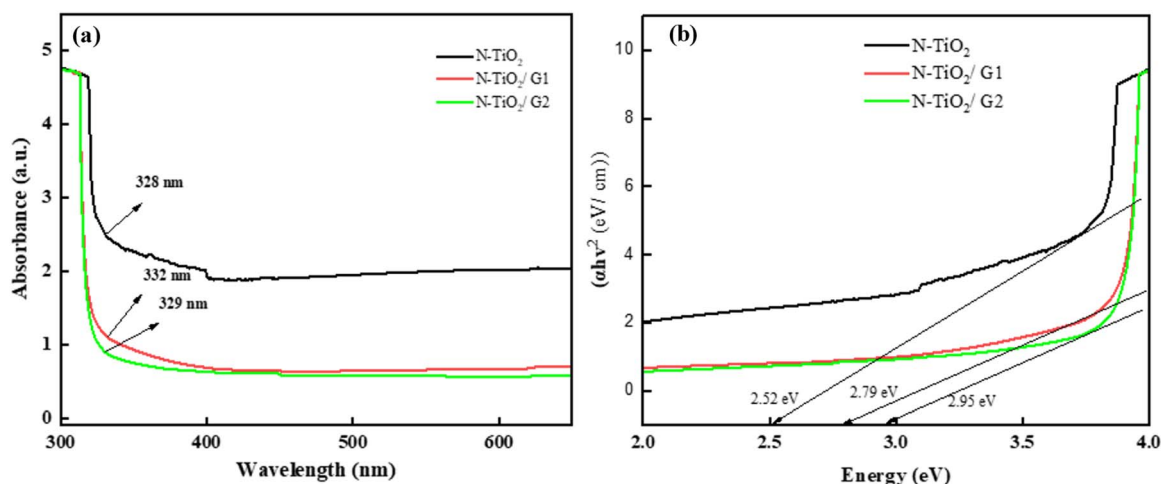

Fig. 6 (a) The UV-vis spectra and (b) Tauc plot of N−TiO₂ and graphene-supported N−TiO₂.

**Table 2** The deconvoluted peaks for O 1s, N 1s and C 1s for N–TiO$_2$ and graphene-supported N–TiO$_2$

O 1s

Sample	Peak I (eV)	Peak II (eV)	Peak III (eV)
N–TiO$_2$	531.85	530.29	532.98
N–TiO$_2$/G1	530.25	531.90	533.20
N–TiO$_2$/G2	529.97	531.37	531.97

N 1s

Sample	Peak I (eV)	Peak II (eV)
N–TiO$_2$	401.36	—
N–TiO$_2$/G1	399.09	401.24
N–TiO$_2$/G2	401.08	—

C 1s

Sample	Peak I (eV)	Peak II (eV)	Peak III (eV)	Peak IV (eV)	Peak V (eV)
N–TiO$_2$	284.77	285.64	286.72	—	—
N–TiO$_2$/G1	283.92	284.79	285.71	286.57	—
N–TiO$_2$/G2	283.82	284.99	286.05	287.16	288.76
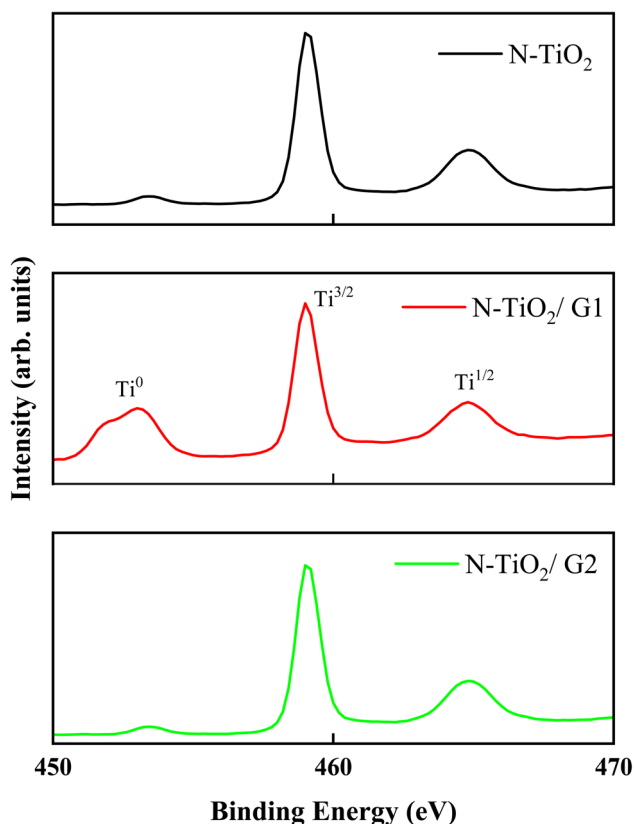
Fig. 7 The Ti 2p core level XPS spectra for N–TiO$_2$ and graphene supported N–TiO$_2$.

N–TiO$_2$ and graphene-supported N–TiO$_2$. The case of pristine N–TiO$_2$ exhibits the blueprint vibrational modes associated with TiO$_2$, where the prominent modes are at 138 cm^{-1} (E$_g$), 195.4 cm^{-1} (E$_g$), 394 cm^{-1} (B$_{1g}$), 515.9 cm^{-1} (A$_{1g}$), and 638.3 cm^{-1} (E$_g$). These values are consistent with recent studies[23] and are attributed to the crystal lattice structures of anatase TiO$_2$.[24] The incorporation of graphene shows increased prominence of E$_g$ vibrational mode appearing at 203 cm^{-1}. The E$_g$ (2) peak position can be attributed to symmetric bending vibration of the O–Ti–O bonds. Hence, the presence of sp^2/sp^3 C–C increases the defect in the crystal structure of TiO$_2$.[25] The increase in sp^2/sp^3 C–C in influencing the lattice structure of N–TiO$_2$ shows a blue shift and red shift in the E$_g$ (1) (138 → 141 → 137 cm^{-1}). The shifts in the E$_g$ (1) can be attributed to the quantum size effect and the occurrence of irregular long-range crystal symmetry from oxygen vacancies.[26]

The light absorption properties of TiO$_2$ provide insight into its light-matter interaction, which is crucial for its applicability in optoelectronics. Fig. 6(a) shows the ultraviolet-visible spectroscopy properties of nitrogenated TiO$_2$ and graphene-supported N–TiO$_2$.

As indicated in the UV-vis spectra, pristine N–TiO$_2$ exhibits absorption in the UVA region at ∼328 nm. The incorporation of graphene as a support for N–TiO$_2$ shows a red shift (328 → 332 nm) and consequent blue shift (332 → 329 nm). The shift in the wavelength absorption suggests formation of mixed phases (anatase/partial rutile phase) and defect formation in the band gap region.[27] The effect of the modification of the lattice structure symmetry is crucial for charge transport properties within the valence and conduction band region.

The Tauc plot shown in Fig. 5(b) depicts a band gap of 2.52 eV for pristine N–TiO$_2$, which is narrower than the pristine TiO$_2$ of 3.0–3.2 eV.[28] The band gap narrowing can be attributed to the formation of states such as O 2p → N 2p, and subsequent N 2p → Ti 3d orbital transitions.[29] The inclusion of graphene in N–TiO$_2$, results in widening of the band gap (2.52 → 2.79 → 2.95 eV). The band gap widening due to C atomic incorporation can be attributed to the reduction of the density of N 2p levels above the valence band and subsequent distortion in the Ti–O bond vibration, where the conduction band minimum increases. The implication of the widened band gap is the ability to detect photons in the UV region, which is significant for deeper UV selectivity.

To further reiterate the electronic structure responsible for band gap engineering, X-ray photoelectron spectroscopy was used to examine the chemical shift of carbon influence on N–TiO$_2$ (see Table 2). The O 1s, N 1s, C 1s and Ti 2p core levels representing the elemental configuration of pristine N–TiO$_2$ and graphene-supported N–TiO$_2$ are shown in Fig. 7 and 8. The Ti 2p core levels for N–TiO$_2$ and graphene-supported TiO$_2$, shown in Fig. 8, describe three distinct states. The Ti 2p core level states for N–TiO$_2$ exhibit three prominent peaks (Ti^0, Ti$^{3/2}$, and Ti$^{1/2}$). The Ti^0 (453.01 eV) state is due to the metallic state of Ti: Ti^{2+}, whereas the Ti$^{3/2}$ and Ti$^{1/2}$ are attributed to the doublet state that is associated with Ti^0 and titanium suboxides.[30] The effect of graphene incorporation shows a slight increase in intensity of the Ti^0 peaks, suggesting increased oxygen
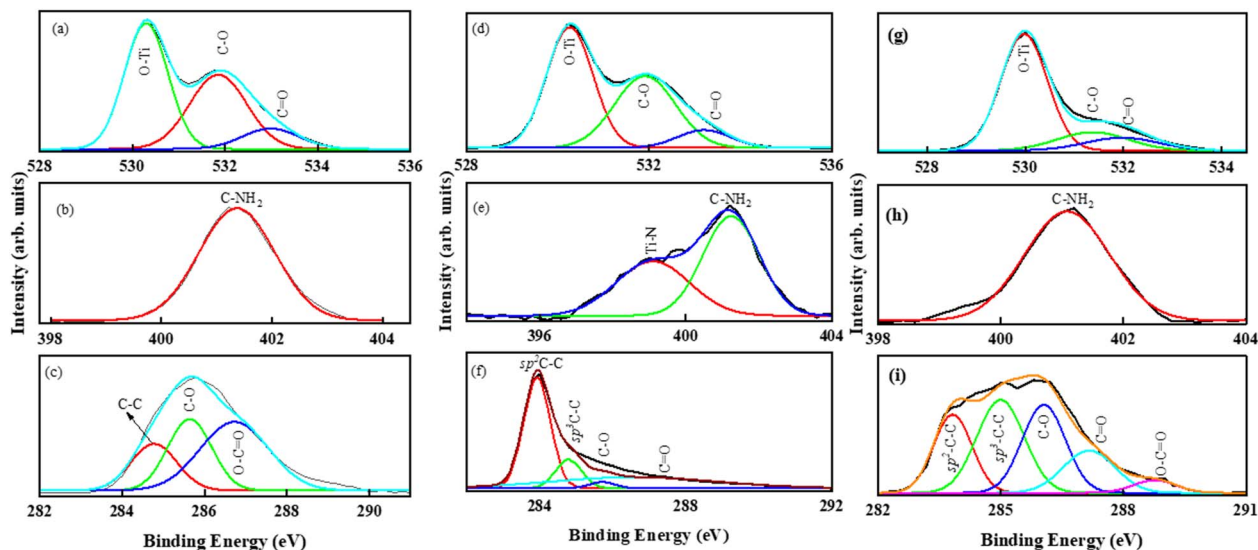
Fig. 8 The XPS spectra for pristine and graphene supported N−TiO$_2$ showing the elemental core levels. (a)−(c) pristine N−TiO$_2$ (d)−(f) NTiO$_2$/G1 (g)−(i) N−TiO$_2$/G2.
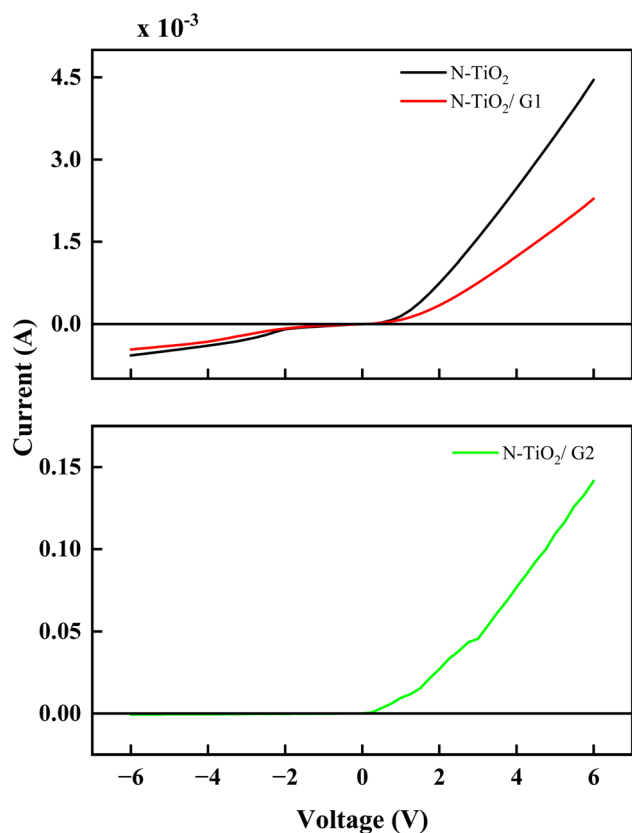

Fig. 9 The current−voltage characteristics of N−TiO$_2$ and graphene supported N−TiO$_2$.
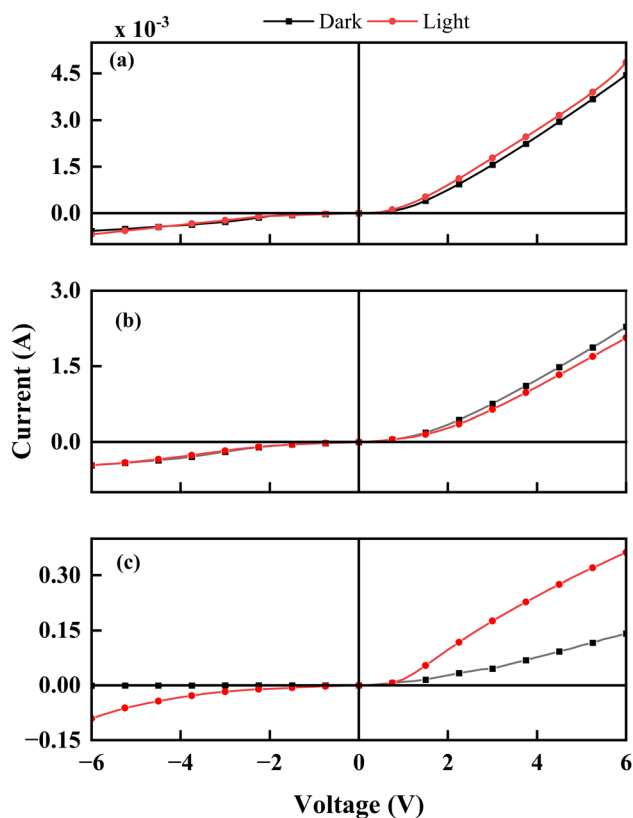

Fig. 10 Photoconductivity properties of pristine (a−c) graphene-supported N−TiO$_2$/G.

vacancies and improved Ti–C/Ti–O–Ti metal–metal interactions. The behaviour of the metal–metal interactions can be significant for photoconductivity performance.

The other core levels of N−TiO$_2$ show the appearance of N 1s, representing the presence of nitrogen that was absent in the EDX mapping. The core levels of O 1s, N 1s and C 1s were deconvoluted into several peak positions as shown in Table 1 to examine the chemical shifts resulting from the electronic
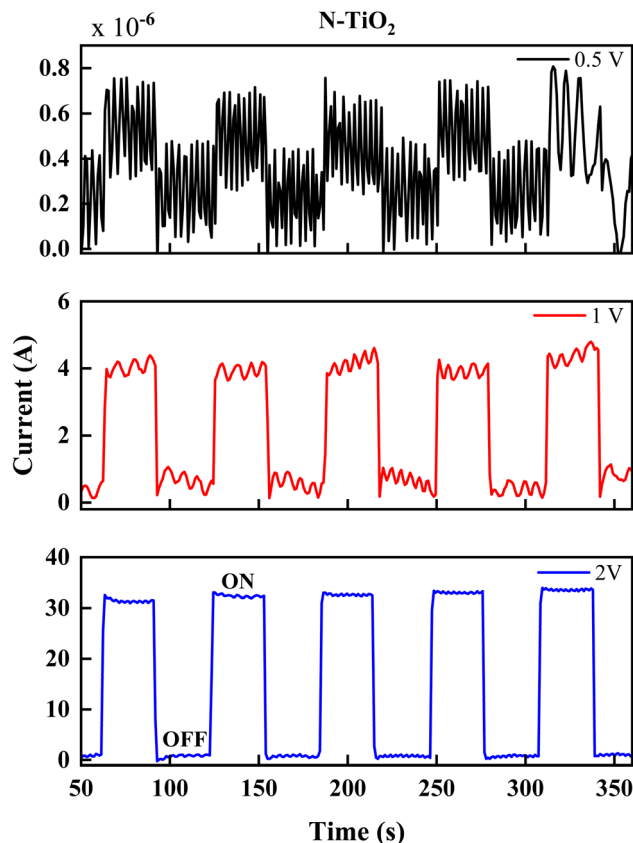
Fig. 11 The photodetection properties of pristine N–TiO$_2$ at 0.5 V, 1 V and 2 V bias voltage.

Fig. 12 The photodetection properties of a low concentration of graphene-supported N–TiO$_2$ at 0.5 V, 1 V and 2 V bias voltage.

interactions. The case of pristine N–TiO$_2$ for the O 1s core level shows three prominent peak positions, located at 531.85 eV, 530.29 eV, and 532.98 eV. The peaks are associated with O–Ti, C–O and C=O bond interactions.[31] The N 1s core levels show one prominent peak, located at 401.36 eV and attributed to N–H/C–NH$_3$ interactions.[32] The C 1s core level interactions exhibit three peaks located at 274.77 eV, 285.64 eV, and 286.74 eV. The deconvoluted C 1s peaks are attributed to C–C, C–O and O–C=O bond interactions, respectively.[33]

The incorporation of low concentration of graphene (N–TiO$_2$/G1) shows chemical shifts towards lower binding energy for O–Ti bond interactions and corresponding shift towards higher binding energy for C–O and C=O bonds. The shift to lower binding energy can be attributed to a decrease in oxygen vacancies around the Ti–O oxidation state, leading to the shifting of the Ti 2p peaks to lower binding energies. Whereas the chemical peak shift for C–O/C=O bond interactions are due to electron density transfer from the C–C, leading to more positively charged electrons.[34] The case of N 1s shows an increase in higher binding energy for N–H and a corresponding formation of Ti–N bond interactions. The formation of the bond structure suggests increased oxygen vacancies, which favours the Ti–N metallic interaction. The resulting bond structure formation is consistent with the mixed states in XRD microstructure (see Fig. 2). Similar behaviour is observed for increased graphene concentrations, where there is shift towards
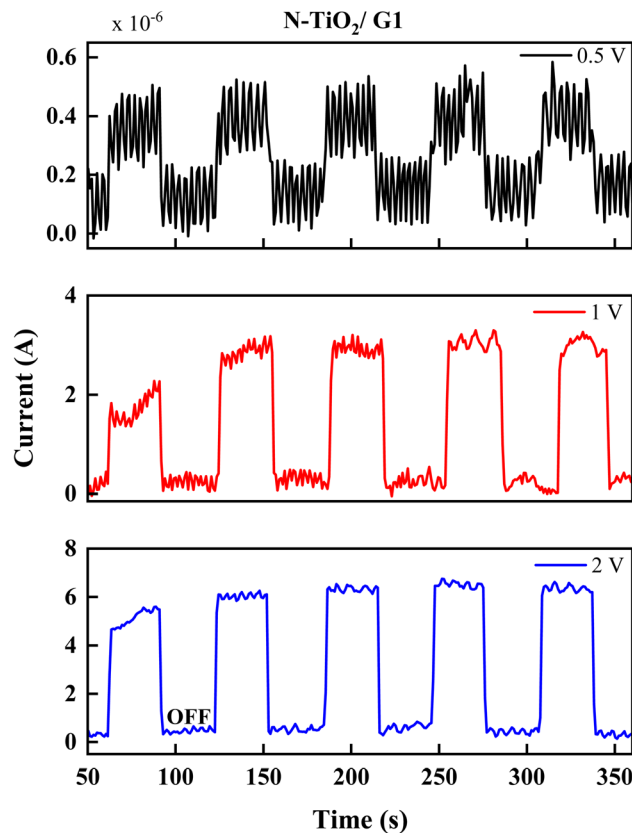
lower binding energies for all three bond interactions. The concentration-dependent shift suggests increased doping effects, which enable further decreased oxygen vacancies with possible increased defect formation. The resulting effect is observed in the additional bond formation at 288.76 eV of C 1s core levels, representing oxidation states of carbonyls (O–C=O). These defect-related bond formations are crucial for light-matter interactions and can be utilized to tune the optoelectronic performance of related devices.

The impact of electronic properties is significant in the electron and hole mobility within the intrinsic band structure of N–TiO$_2$. The significance of electron mobility is evident in the electrical conductivity properties of the N–TiO$_2$ nanomaterial. Using the fabricated device shown in Fig. 1, the electrical conductivity properties of the N–TiO$_2$ and graphene-supported N–TiO$_2$ were examined.

Fig. 9 shows the current–voltage characteristics of pristine and graphene-supported N–TiO$_2$. The case of pristine N–TiO$_2$ shows asymmetric features, depicting of a typical semiconductor behaviour, where the majority carriers are aligned in the forward bias direction. The features exhibit highly conductive behaviour, which is in proximity to previous reports of typical anatase TiO$_2$.[35] Although typical TiO$_2$ exhibits symmetric n-type conductivity features,[36] the nitrogenation process enables charge transfers in the forward bias direction. The incorporation of low concentrations of graphene into N–TiO$_2$ results in a slight decrease in electrical conductivity and
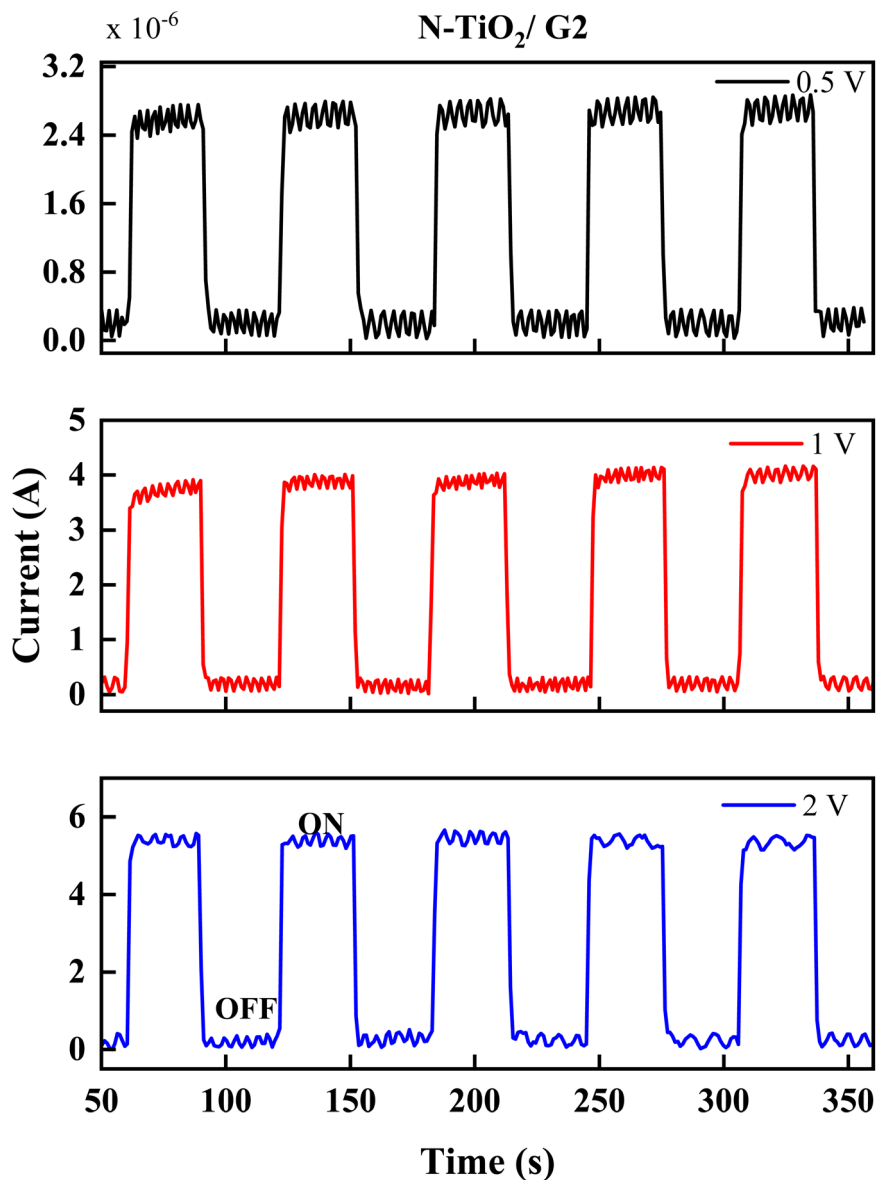
Fig. 13 The photodetection properties of a high concentration of graphene-supported N−TiO$_2$ at 0.5 V, 1 V and 2 V bias voltage.

a corresponding reduction in minority carriers in the reverse bias direction. The slight decrease can be attributed to a widening depletion region, where the flow of majority carriers is suppressed, resulting in a corresponding increase in the barrier for carrier injection.[37,38] The increase in graphene concentration in N−TiO$_2$ shows almost complete annihilation of the minor charge carrier activities in the reverse bias. The significant reduction in minority carrier activity can be attributed to the effect of charge carrier recombination, where graphene accelerates recombination at the interface, further reducing the minority carrier concentration in reverse bias. The rectification ratios for N−TiO$_2$, N−TiO$_2$/G1, and N−TiO$_2$/G2 were calculated to be 5.2, 3.8, and 17.3, respectively. Hence, graphene can be utilized to drive p-type charge transfer features, which could be significant for optimized device performance.

The impact of illumination on influencing the charge transport behaviour can be used to examine the light-matter interaction behaviour, which is crucial for optoelectronic applications. The fabricated devices were examined under various light conditions to determine the effects of illumination. Fig. 10 shows the comparison of electrical conductivity responses under dark and light conditions. As indicated for pristine N−TiO$_2$ (a), there is a slight increase in major carriers in the forward bias with negligible activity in the reverse bias. The increase in photoconductivity response for N−TiO$_2$ can be attributed to the photon excitations. The increased majority carriers (electrons) are photoexcited from the valence band to the conduction band, which leads to increased majority carrier (electron) concentration in the forward bias. Low concentrations of graphene incorporation show a nontrivial behaviour with a slight decrease in the photoconductivity response. The behaviour can be attributed to charge suppression, owing to photo-generated electrons in TiO$_2$ being transferred to graphene due to favourable energy alignment. Furthermore, the
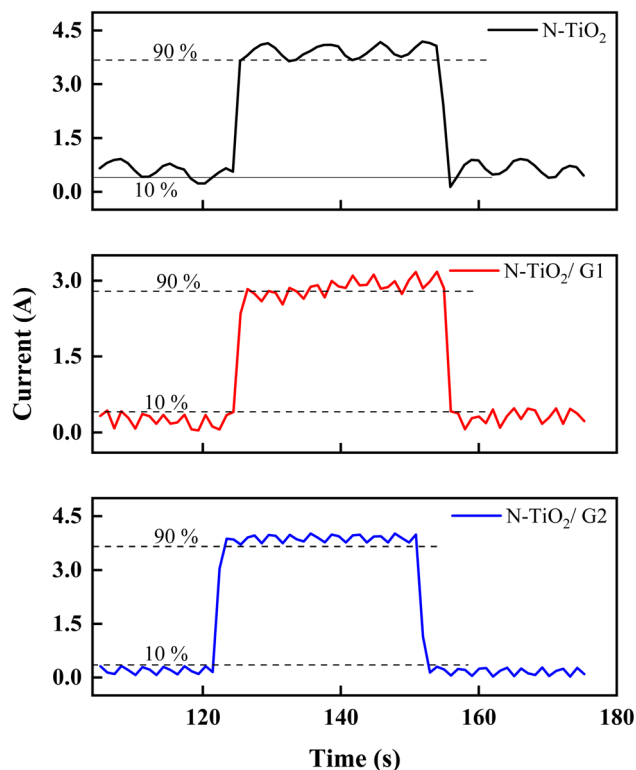
Fig. 14 The response characteristics of pristine and graphene-supported N–TiO$_2$ at 1 V bias voltage.

Table 3 The extrapolated photosensitivity and response times of pristine and graphene-supported N–TiO$_2$

Sample	Response time	Recovery time	Current gain	Photosensitivity
N–TiO$_2$	4.31	1.71	8.02	7.02
N–TiO$_2$/G1	3.12	1.71	9.14	8.14
N–TiO$_2$/G2	1.63	1.53	8.78	7.78

presence of graphene acts as a barrier, where charge separation depletes the majority carriers near the interface. The case of increase graphene concentration shows the trivial case, where there is an increase in both forward and reverse bias directions. The increase carrier concentration in both directions suggests increased redistribution of the electron–hole conditions, resulting from photoexcitation of the charges.

The photodetection properties of pristine and graphene-supported N–TiO$_2$ were examined using bias voltages of 0.5 V, 1 V and 2 V. The current–time characteristics are shown in Fig. 11–13.

The case of pristine N–TiO$_2$ shows improved photoresponse at 2 V bias voltage, which suggests enhanced diode-like behavior, allowing the easy flow of current one direction than the other under illumination. The behaviour can be attributed to increased electric field across the N–TiO$_2$ interface and improved separation and collection of photogenerated electron–hole pairs, resulting in enhanced photocurrent.[39] The

incorporation of low graphene concentrations (see Fig. 11) slightly improves the photoresponse of the photodetection, especially at low voltage bias (0.5 V). The slight improvement can be attributed to the charge separation feature contribution from graphene.[40]

The high concentration of graphene in N–TiO$_2$ (see Fig. 13) results in a significant improvement of the photodetector device's photoresponse. The performance at a low bias voltage (0.5 V) indicates an enhanced photoresponse compared to both pristine N–TiO$_2$ and N–TiO$_2$/G1. The improvement in the photoresponse can be attributed to the modified intrinsic potential and depletion layer width, where carrier separation is improved,[41] owing to increased graphene presence. This leads to minimal external voltage requirements to drive the flow of electrons in the desired direction.

Fig. 14 shows the response characteristics of pristine and graphene-supported N–TiO$_2$ at 1 V bias voltage, whereas Table 3 depicts the calculated values using the expression found elsewhere.[7] The photosensitivity and response time for pristine N–TiO$_2$ are calculated as 4.31 s and 7.02, respectively. The incorporation of graphene showed a steady decrease in the response time and a corresponding 14.7% improvement in the photosensitivity. These values are in proximity to recent values of 0.7 s that employed a higher bias voltage of 2.5 V.[42] The response and recovery times significantly reduce with graphene concentration due to the high charge separation ability of graphene.[40] Additionally, the sensitivity appears to increase up to an optimum point, where it then saturates before decreasing. Important to note that performance improvement does not necessarily originate from the irradiation absorption of graphene but rather to the efficient charge separation by graphene.[40] Hence, the incorporation of graphene into N–TiO$_2$ can drive the efficiency of TiO$_2$-based photodetectors.

Furthermore, the transport mechanism that accounts for the electrical conductivity and photosensitivity of N–TiO$_2$ supported graphene can be reiterated using band alignment diagrams as proposed by AlShammari et al.[43]. Fig. 15 shows the proposed energy band alignment for the Ag/N–TiO$_2$–rGO/Ag device under both dark and UV-illuminated conditions. In this structure, N–TiO$_2$ functions as an n-type semiconductor, while rGO acts as the p-type counterpart, with Ag (work function ≈ 4.28 eV) serving as the electrical contact. Under dark conditions (Fig. 9(a)), charge transport is predominantly governed by the intrinsic carriers of N–TiO$_2$ and rGO. Upon UV illumination (Fig. 8(b)), photoexcitation within N–TiO$_2$ generates electron–hole pairs, which are believed to migrate across the N–TiO$_2$/rGO interfaces, forming two p–n junctions accompanied by corresponding depletion regions. The internal electric fields established in these regions facilitate the directional movement of electrons toward N–TiO$_2$ and holes toward rGO, thereby enhancing charge separation and minimizing recombination. Furthermore, the relatively high Fermi level of rGO (∼4.5 eV) is expected to aid hole extraction and induce downward band bending near the N–TiO$_2$/Ag interface, effectively reducing the hole injection barrier. Although rGO does not directly contribute to electron–hole pair generation, it significantly
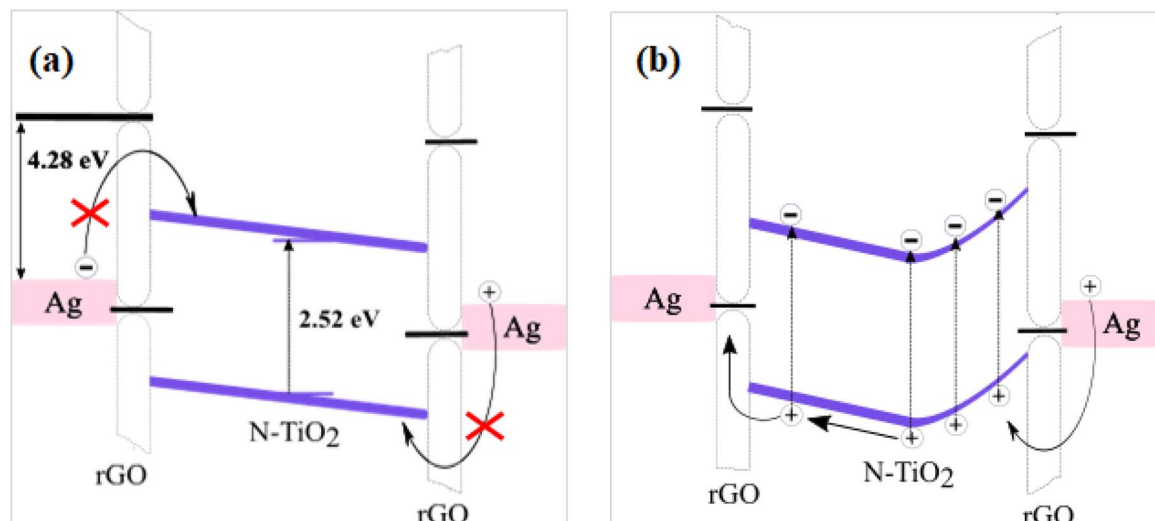
Fig. 15 The band alignment diagram for N−TiO₂-supported graphene showing the charge transport properties. (a) The transfer of charges from Ag contacts to the active materials and (b) active material to the Ag contact.

improves carrier transport, thereby enhancing both the photo-current and photosensitivity of the device.

Conclusions

The current study employed concentrations to establish the photoresponse of N–TiO₂ using a hydrothermal synthesis approach. The microstructure properties of pristine and graphene N–TiO₂ suggested a mixed phase of TiN/anatase TiO₂. The formation of novel bond interactions from the XPS analysis suggests increased orbital states, owing to contributions from graphene incorporation into N–TiO₂. The improved photo-response and improved response times of graphene-supported N–TiO₂ are attributed to photoexcited electrons, as well as improved charge separation in the band region. The study has established that the fabricated TiO₂/graphene composite as a low-power and sensitive photodetector device.

Conflicts of interest

The authors declare no conflicts of interest.

Data availability

The data that supports the current research can be made available upon reasonable request to the corresponding author.

Acknowledgements

References

1 A. Kumar, M. A. Khan and M. Kumar, *J. Phys. D: Appl. Phys.*, 2021, **55**, 133002.
2 P. K. Yadav, B. Ajitha, Y. A. K. Reddy and A. Sreedhar, *Chemosphere*, 2021, **279**, 130473.
3 Y.-C. Huang, V. Parimi, W.-C. Chang, H.-J. Syu, Z.-C. Su and C.-F. Lin, *IEEE Photonics J.*, 2021, **13**, 1–7.
4 L. Shi and S. Nihtianov, *IEEE Sens. J.*, 2012, **12**, 2453–2459.
5 H. Liu, Z.-X. Liu, S. Wang, J. Huang, H. Ju, Q. Chen, J. Yu, H. Chen and C.-Z. Li, *Adv. Energy Mater.*, 2019, **9**, 1900887.
6 C. Luo, C. Xu, L. Lv, H. Li, X. Huang and W. Liu, *RSC Adv.*, 2020, **10**, 8385–8395.
7 D. O. Idisi, U. O. Aigbe, D. Chilukusha, B. W. Mwakikunga and J. K. O. Asante, *Diamond Relat. Mater.*, 2024, **149**, 111584.
8 S. Ge, D. Sang, L. Zou, Y. Yao, C. Zhou, H. Fu, H. Xi, J. Fan, L. Meng and C. Wang, *Nanomaterials*, 2023, **13**, 1141.
9 Y. Etafa Tasisa, T. Kumar Sarma, R. Krishnaraj and S. Sarma, *Results Chem.*, 2024, **11**, 101850.
10 Y. Zhou, Y. Wang, Y. Wang, H. Yu, R. Zhang, J. Li, Z. Zang and X. Li, *ACS Appl. Mater. Interfaces*, 2021, **13**, 56485–56497.
11 M. I. EL-Henawey, M. Kubas, A. H. Oraby, A. El-Shaer, M. Abdelfatah and H. Y. Salah, *Opt. Mater.*, 2024, **156**, 115955.
12 P. F. Lim, K. H. Leong, L. C. Sim, A. Abd Aziz and P. Saravanan, *Environ. Sci. Pollut. Res.*, 2019, **26**, 3455–3464.
13 A. Aykaç, H. Gergeroglu, B. Beşli, E. Ö. Akkaş, A. Yavaş, S. Güler, F. Güneş and M. Erol, *Nanoscale Res. Lett.*, 2021, **16**, 65.
14 S. Noothongkaew, O. Thumthan and K.-S. An, *Mater. Lett.*, 2018, **218**, 274–279.
15 S. Ullbrich, J. Benduhn, X. Jia, V. C. Nikolis, K. Tvingstedt, F. Piersimoni, S. Roland, Y. Liu, J. Wu, A. Fischer, D. Neher, S. Reineke, D. Spoltore and K. Vandewal, *Nat. Mater.*, 2019, **18**, 459–464.

16 P. Wen, C. Cai, H. Zhong, L. Hao and X. Xu, *J. Mater. Sci.*, 2015, **50**, 5944–5951.

17 X. Kan, C. Deng, C. Yu, J. Ding and H. Zhu, *J. Mater. Sci.: Mater. Electron.*, 2018, **29**, 10624–10630.

18 L. Hu, J. Wang, J. Zhang, Q. Zhang and Z. Liu, *RSC Adv.*, 2014, **4**, 420–427.

19 C. Parvathiraja, S. Katheria, M. R. Siddiqui, S. M. Wabaidur, M. A. Islam and W.-C. Lai, *Catalysts*, 2022, **12**, 834.

20 F. K. M. Alosfur, A. A. Ouda, N. J. Ridha and S. H. Abud, in *AIP Conference Proceedings*, AIP Publishing, 2019, vol. 2144.

21 J. M. Abisharani, R. DineshKumar, S. Devikala, M. Arthanareeswari and S. Ganesan, *Mater. Res. Express*, 2020, **7**, 025507.

22 P. Wang, H. Li, Y. Cao and H. Yu, *Acta Phys.-Chim. Sin.*, 2021, **37**, 2008047.

23 M. Lubas, J. J. Jasinski, M. Sitarz, L. Kurpaska, P. Podsiad and J. Jasinski, *Spectrochim. Acta, Part A*, 2014, **133**, 867–871.

24 G. Kaur, P. Negi, R. J. Konwar, H. Kumar, N. Devi, M. Ranjan, K. P. Sooraj, H. Trivedi, B. Rajyaguru, N. P. Barde, P. P. Bardapurkar, N. A. Shah and P. S. Solanki, *Opt. Mater.*, 2025, **162**, 116851.

25 S. H. Saknure, A. D. Bokhare and A. C. Kumbharkhane, *Cellulose*, 2025, **32**, 8757–8765.

26 D. Li, L. Deng, H. Chen, X. Song, C. Chen, Y. Feng, H. Bai, Y. Qin, W. Zhang and C. Li, *Langmuir*, 2025, **41**, 6007–6019.

27 D. K. Muthee, F. B. Dejene and L. K. Munguti, *Appl. Catal., A*, 2025, **695**, 120166.

28 S. Munir, S. M. Shah, H. Hussain and R. Ali khan, *Mater. Des.*, 2016, **92**, 64–72.

29 T. Xu, M. Wang, T. Wang and J. Wuhan Univ, *Technol.-Mat. Sci. Edit.*, 2019, **34**, 55–63.

30 W.-C. Peng, Y.-C. Chen, J.-L. He, S.-L. Ou, R.-H. Horng and D.-S. Wuu, *Sci. Rep.*, 2018, **8**, 9255.

31 X. Yu, Y. Li, C. Pei, Y. Lu, J. K. Kim, H. S. Park and H. Pang, *Adv. Sci.*, 2024, **11**, 2310013.

32 M. Šetka, R. Calavia, L. Vojkůvka, E. Llobet, J. Drbohlavová and S. Vallejos, *Sci. Rep.*, 2019, **9**, 8465.

33 B. Lesiak, L. Kövér, J. Tóth, J. Zemek, P. Jiricek, A. Kromka and N. Rangam, *Appl. Surf. Sci.*, 2018, **452**, 223–231.

34 S. J. Gerber and E. Erasmus, *Mater. Chem. Phys.*, 2018, **203**, 73–81.

35 R. Lahiri, A. Ghosh, S. M. M. D. Dwivedi, S. Chakrabartty, P. Chinnamuthu and A. Mondal, *Appl. Phys. A*, 2017, **123**, 573.

36 P. S. M. Saad, H. B. Sutan, S. S. Shariffudin, H. Hashim and U. M. Noor, in *IOP Conference Series: Materials Science and Engineering*, IOP Publishing, 2015, vol. 99, p. 012006.

37 A. Hazra and P. Bhattacharyya, *IEEE Trans. Electron Devices*, 2015, **62**, 1984–1990.

38 P. Cui and Y. Xue, *Mater. Sci. Semicond. Process.*, 2022, **139**, 106323.

39 D. Pan, D. Jiao, Z. Li, Y. Guo, C. Feng, Y. Liu, L. Wang and M. Wu, *ACS Sustain. Chem. Eng.*, 2015, **3**, 2405–2413.

40 C. Zhou, X. Wang, X. Kuang and S. Xu, *J. Manuf. Syst.*, 2016, **26**, 075003.

41 H. Deng, C. Qin, K. Pei, G. Wu, M. Wang, H. Ni and P. Ye, *Mater. Chem. Phys.*, 2021, **270**, 124796.

42 J. Zou, Q. Zhang, K. Huang and N. Marzari, *J. Phys. Chem. C*, 2010, **114**, 10725–10729.

43 A. S. AlShammari, M. M. Halim, F. K. Yam and N. H. M. Kaus, *Results Phys.*, 2020, **19**, 103630.